John M. Boone, PhD
Thomas R. Nelson, PhD
Karen K. Lindfors, MD
J. Anthony Seibert, PhD

Dedicated Breast CT: Radiation Dose and Image Quality Evaluation[1]

Index terms:
Breast neoplasms, CT, 00.1211
Breast neoplasms, radiography, 00.11
Breast radiography, radiation dose
Computed tomography (CT), radiation exposure, 00.1211

Published online before print
10.1148/radiol.2213010334
Radiology 2001; 221:657–667

Abbreviations:
AGD = average glandular dose
CNR = contrast-to-noise ratio
kVp = peak kilovoltage
LAC = linear attenuation coefficient
mAs = milliampere second
$\sigma_{CT\#}$ = average noise
SNR = signal-to-noise ratio

[1] From the Department of Radiology, X-ray Imaging Laboratory, University of California, Davis Medical Center, 4701 X St, Sacramento, CA 95817 (J.M.B., K.K.L., J.A.S.); and Department of Radiology, University of California, San Diego (T.R.N.). From the 2000 RSNA scientific assembly. Received January 18, 2001; revision requested March 16; revision received April 10; accepted May 14. Supported in part by grants from the U.S. Army Breast Cancer Research Program (DAMD17-98-1-8176) and the National Cancer Institute (R21 CA82077). **Address correspondence to** J.M.B. (e-mail: *jmboone@ucdavis.edu*).

Author contributions:
Guarantor of integrity of entire study, J.M.B.; study concepts and design, J.M.B., T.R.N.; literature research, J.M.B.; experimental studies, J.M.B., J.A.S.; data acquisition, J.M.B., J.A.S.; data analysis/interpretation, all authors; statistical analysis, J.M.B.; manuscript preparation, J.M.B.; manuscript definition of intellectual content, editing, and revision/review, all authors; manuscript final version approval, J.M.B.

PURPOSE: To evaluate the feasibility of breast computed tomography (CT) in terms of radiation dose and image quality.

MATERIALS AND METHODS: Validated Monte Carlo simulation techniques were used to estimate the average glandular dose (AGD). The calculated photon fluence at the detector for high-quality abdominal CT (120 kVp, 300 mAs, 5-mm section thickness) was the benchmark for assessing the milliampere seconds and corresponding radiation dose necessary for breast CT. Image noise was measured by using a 10-cm-diameter cylinder imaged with a clinical CT scanner at 10–300 mAs for 80, 100, and 120 kVp. A cadaveric breast was imaged in the coronal plane to approximate the acquisition geometry of a proposed breast CT scanner.

RESULTS: The AGD for 80-kVp breast CT was comparable to that for two-view mammography of 5-cm breasts (compressed breast thickness). For thicker breasts, the breast CT dose was about one-third less than that for two-view mammography. The maximum dose at mammography assessed in 1-mm^3 voxels was far higher (20.0 mGy) than that at breast CT (5.4 mGy) for a typical 5-cm 50% glandular breast. CT images of an 8-cm cadaveric breast (AGD, 6.3 mGy) were subjectively superior to digital mammograms (AGD, 10.1 mGy) of the same specimen.

CONCLUSION: The potential of high signal-to-noise ratio images with low anatomic noise, which are obtainable at dose levels comparable to those for mammography, suggests that dedicated breast CT should be studied further for its potential in breast cancer screening and diagnosis.

Mammography is used for breast cancer screening throughout the world, and the recent reduction in breast cancer mortality is largely attributed to earlier detection (1–3). Despite this success, many investigators have proposed non–x-ray screening approaches in hopes of achieving even earlier breast cancer detection. The imaging technologies explored for breast cancer detection include scintimammography (4,5), positron emission tomography (6,7), magnetic resonance imaging (8,9), optical imaging (10), microwave imaging (11), and ultrasonography (12). Each approach has advantages and disadvantages, but so far, no other modality has been able to compete with mammography in terms of detection performance, noninvasiveness, imaging time, and cost-effectiveness. Consequently, many of these other imaging examinations are used in the clinical setting after a screening mammogram or clinical breast examination has revealed a possible abnormality.

Despite its utility, mammography is not without limitations (13). The most widely cited downfall of mammography is its reduced sensitivity in women with dense breasts (14–16). Imaging of the dense breast with good sensitivity has become more important as younger women have begun to undergo screening routinely, as the use of hormone replacement therapy has expanded, and as genetic testing has begun to identify younger women at high risk. Digital mammography systems (17,18) that have a wider dynamic range than screen-film mammography have been developed, in part to address the increased challenges of imaging the dense breast. Early results indicate that digital mammography may lead to important incremental improvement in cancer detection in dense breasts.

Although computed tomography (CT) was studied in passing for its utility in breast cancer screening some years ago (19–22), this modality has been largely dismissed as having a

practical role in breast cancer screening due to concerns about radiation dose and cost-effectiveness. Most earlier studies involved conventional CT scanner technology, in which the images were acquired transversely and thus the x-ray beam had to penetrate the thoracic cavity. With this geometry, not only is a large amount of nonbreast tissue exposed to radiation, leading to substantial radiation dose inefficiency, but also cardiac and respiratory motion have the potential to reduce image quality.

Despite the conventional wisdom that CT is not effective for breast cancer screening, it is generally accepted that CT is far better than projection radiographic techniques in terms of contrast resolution by a factor of about 10 (23). When the complex normal anatomy (structured noise) of the dense breast is factored into the analysis of contrast resolution, the tomographic nature of CT facilitates the ability to eliminate overlapping structures, which are problematic in conventional mammography.

The purpose of this investigation was to evaluate the feasibility of breast CT in terms of radiation dose and image quality. Although a host of other considerations, such as diagnostic accuracy, cost, and interpretation time, remain to be evaluated, dose and image quality are fundamental to the potential of dedicated breast CT. Thus, we believe this investigation represents a necessary first step in assessing the potential of breast CT.

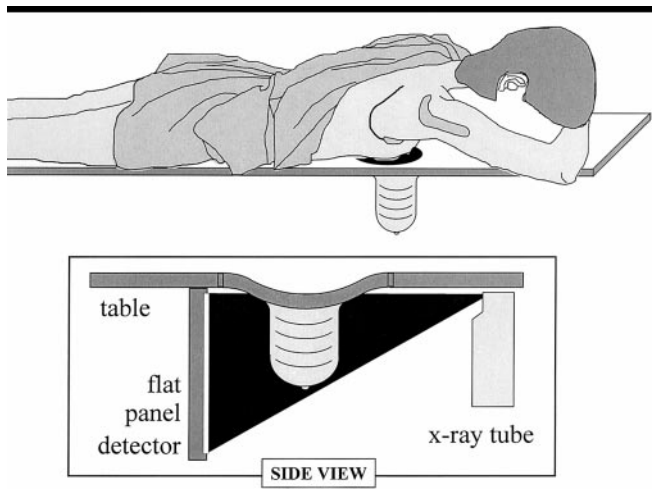

Figure 1. Drawings illustrate the geometry of a CT scanner customized for breast imaging, at which the breast would be imaged in the pendulant position. The inset (bottom) is a side-view close-up, which demonstrates that a swale in the table may allow imaging closer to the chest wall.

MATERIALS AND METHODS

CT Scanner Geometry

A plausible design for a CT scanner tailored specifically for breast cancer screening is shown in Figure 1. The scanner should prevent the exposure of tissues in the thoracic cavity; thus, CT would need to be performed in the coronal plane. Each breast would be scanned individually with the woman lying prone on the table and the breast to be imaged hanging through a hole in the table, a geometry similar to that of presently available digital breast biopsy systems. With the breast hanging in the pendulant position, the x-ray tube and detector arrays would rotate around the breast in the horizontal plane. To ensure that breast tissues close to the chest wall and in the axilla are imaged, the x-ray tube and detectors would have to be positioned just below the bottom of the shielded table. The table surface surrounding the cutout for the breast would be engineered with a swale to allow a portion of the chest wall to extend into the scanner field of view and thus enable adequate coverage of the breast, as shown in the box inset in Figure 1. Gentle pressure beyond gravity would be applied to immobilize the breast and pull the breast tissue away from the chest wall, but the breast compression used in mammography would not be necessary.

The coronal acquisition geometry of the dedicated breast CT scanner would allow the reconstructed CT images to be sized to the dimensions of the breast. For example, for a 15-cm-diameter field of view, a 512 × 512 CT image would have pixel dimensions close to 300 μm. With CT, there is a trade-off between image noise and voxel volume, and there probably is little clinical motivation to acquire sections with thicknesses of less than 1 mm when standard two-dimensional viewing is used, since this will increase image noise and generate more images to interpret. Isotropic resolution (eg, 300 × 300 × 300-μm voxels), however, might be useful in concert with three-dimensional viewing techniques and could be achieved by using cone-beam techniques (24) with flat panel detectors (25,26). For routine breast CT scanning, the section thickness probably would be on the order of 1–2 mm.

The pendulant breast would be approximately cylindrical, with slight tapering of the diameter anteriorly. The dimensions of the cylindrical breast were estimated on the basis of the assumptions illustrated in Figure 2. The breast dimensions of a small cohort of 82 women were evaluated in our breast clinic on the basis of measurements made on the screen-film images. Human use authority (with exemption under category 4) was obtained for this activity. During normal mammographic interpretation, a mammographer (K.K.L.) measured the width of the left breast image at the edge of the film that corresponded to the width of the compressed breast near the chest wall and recorded this dimension on a form. The compressed breast thickness, which was printed onto the film, also was recorded.

Monte Carlo Simulations

Previously validated (27,28) Monte Carlo techniques were used to assess the radiation dose levels for dedicated breast CT. The SIERRA (Simple Investigational Environment for Radiology Research Applications) (27,28) code was modified to emulate the acquisition geometry of a dedicated breast CT scanner. The influence of the x-ray spectrum was explicitly evaluated as part of the simulation process. To estimate the appropriate amount of filtration for breast CT, x-ray spectral properties were measured with a commercial CT scanner (Lightspeed; GE Medical Systems, Milwaukee, Wis) at our institution.

With the CT gantry in the "parked" position (achieved with assistance from service personnel), the half value layer was determined by using type 1100 aluminum and an ionization chamber (Triad; Keithley, Cleveland, Ohio) for 80, 120, and 140 kVp. The output of the CT x-ray tube (air kerma per milliampere second [mAs] at the isocenter) also was measured. By using a spectral model appropriate for CT (29), we mathematically varied the amount of added aluminum filtration until the mod-

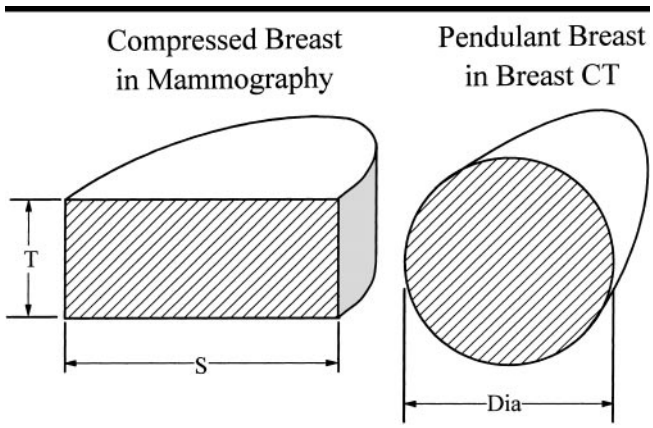

Figure 2. Drawings illustrate the geometry of the breast at mammography and breast CT. *Dia* = diameter, *S* = width of the breast at the edge of the mammogram, *T* = thickness of the compressed breast. The areas of the striped region on both diagrams are the same. These shapes were used to convert compressed breast thickness at mammography to breast diameter at CT.

eled spectra matched both the half value layer and the output measurements of the commercial scanner. The filtered spectral model was then used to produce x-ray spectra from 30 to 140 kVp in the Monte Carlo simulations.

With CT, the dose required to obtain a transverse section at a given peak kilovoltage (kVp) is linearly related to the product of the x-ray beam current (in milliampere) and the acquisition time (in seconds); this product is commonly referred to as the mAs. Because the mAs is a part of the technique protocol for any CT scanner, it was used in this study as a descriptor of x-ray beam quantity. Two authors (J.A.S., J.M.B.) determined the relationship between the output of the x-ray tube (in milligray or milliroentgen) and the photon fluence at the isocenter of the commercial CT scanner, as a function of the mAs, at each kVp by using physical exposure measurements combined with spectral modeling techniques.

Radiation dose was computed by using a cylindrical breast geometry with diameters ranging from 6 to 16 cm, which span the range of breast sizes that probably would be encountered clinically. A breast composition of 50% glandular tissue and 50% adipose tissue (ie, "50/50 breast") was simulated by using the data of Hammerstein et al (30). The isocenter is the position in space around which the x-ray tube and detector arrays rotate, and was assumed to be coincident with the center of the breast cylinder. The x-ray source–to-isocenter distance was assumed to be 54 cm, which is similar to the x-ray source–to-isocenter distance in a clinical CT scanner at our institution. A fan beam of x rays was incident on the right cylinder, with a 1-mm-thick fan beam positioned orthogonally to the central axis of the cylinder. The x-ray source was rotated in the simulation 360° around the breast cylinder in 3° increments, for a total of 120 different source positions. For each simulated x-ray spectrum (ie, kVp) and breast diameter, a total of 10,000,000 x-ray photons were tracked, and the energy deposition in a grid of 1 × 1 × 20-cm voxels was tallied.

The mean breast radiation dose and SD were computed from 10 Monte Carlo runs of 1,000,000 photons each, and these data were used to compute the coefficient of variation (ie, ratio of the SD to the mean). To evaluate dose homogeneity, the dose distribution was computed by using 1 mm × 1 mm × 20 cm voxels. The out-of-plane scattered radiation dose, regardless of its distance from the collimated CT section, as well as the primary dose deposition, were tallied. This acquisition geometry is equivalent to the measurement of the multisection average dose, which the CT dose index seeks to approximate (31). The CT dose index is the standard measurement used by the CT industry (by Federal statute) and by medical physicists (by convention) to assess CT radiation dose.

The energy deposition of ionizing radiation due to photoelectric interaction and Compton scattering events was tallied in each tissue voxel by a computer program written by one of the authors (J.M.B.). Rayleigh interactions also were tracked, but these do not result in energy deposition in the medium. The dose delivered to the medium studied was corrected to the glandular tissue dose by using the energy-dependent ratio of the mass energy attenuation coefficient of glandular tissue to the mass energy attenuation coefficient of the medium. This correction was performed on an interaction-by-interaction basis. The tallied energy (in joules) in each voxel was normalized by the mass of each voxel (in kilograms) to determine the average glandular dose (AGD, in milligrays). With use of the established relationship between photon fluence and mAs at each kVp, the dose was then normalized to correspond to that delivered by using 100 mAs. The resulting dose values were essentially CT dose index determinations, in milligrays per 100 mAs. The AGD delivered at other mAs settings could then be easily computed from these data.

To compute the radiation dose for a breast CT study, an estimate of the mAs needed at each kVp to produce clinically useful images was required. Since the typical photon fluence levels at the CT detector (which largely determine the signal-to-noise ratio [SNR] on the image) were unknown to us, we used the example of a typical CT technique that is known to produce images with a high SNR. A nonhelical abdominal CT technique performed with 120 kVp, 300 mAs, 5-mm section thickness, and a 32-cm-diameter cylindrical water-equivalent phantom was simulated. This technique was used in a computer simulation to determine the photon fluence striking the center of the CT detector array, integrated over a 360° rotation of the scanner. To maintain the same SNR in breast CT as that in the abdominal CT benchmark, the same photon fluence should be incident on the detector arrays. A simulation was performed for various diameters (6–16 cm) of cylinders with a 50% glandular tissue composition. The mAs necessary to deliver the same photon fluence to the detector behind the breast for a 1-mm-thick CT image was evaluated for x-ray spectra between 40 and 140 kVp.

The heterogeneity in dose for mammography and breast CT was evaluated (J.M.B.) by using 1-mm^3 voxels, and for mammography, a rectangular cross-sectioned breast was simulated. The Monte Carlo techniques described previously were used to assess the dose distribution at CT; however, for mammography, the task was slightly more difficult due to the orthogonal compression used at two-view mammography. To simplify this computation, mammographic exposure to a rectangular breast (in coronal cross section) was simulated. The rectangular shape simplified the application of mathematical compression, as described in the following text.

A 50% glandular 5-cm compressed breast thickness was used, and the median breast width determined from breast size analyses was assumed for the width dimension. In addition, a 4-mm skin layer was assumed (32). Under compression, the cross section of the breast was modeled as a 5.0 × 19.4-cm rectangle, and when uncompressed, the breast cross section was warped by using bilinear interpolation to a 9.85 × 9.85-cm square, which is equal in area to the rectangle. Monte Carlo techniques were used to determine the dose deposition to the rectangular cross section of the breast, and the resulting Monte Carlo depth-dose curve was computer fit by using commercial software (Table Curve 2D; Jandel Scientific, Corte Madera, Calif). After breast exposure in one direction (eg, craniocaudal), the rectangular breast was warped to a square and then warped to a rectangle in the orthogonal direction (19.4 × 5.0 cm) for a second (eg, mediolateral oblique) exposure.

For dose distribution analysis, the breast was warped back to the square orientation. A 26-kVp molybdenum anode x-ray spectrum (33) filtered with 0.030-mm molybdenum and 3-mm poly (methyl methacrylate) (PMMA) (the compression paddle) was used. The entrance skin exposure used in this computation (17.5 mGy air kerma or 2,000 mR) was determined by means of interpolation from technique data measured at our institution for 50% glandular phantoms. For dose comparisons, an 11-cm-diameter breast (equal area) was simulated for exposure by using the breast CT geometry described earlier.

Experimental Studies

A 10-cm-diameter PMMA cylinder, 10 cm in length, was fabricated for this project. The cylinder had two 12.7-mm-diameter holes machined into it to accommodate a CT ionization pencil chamber: One hole was at the center, and one was centered 19 mm from the edge of the cylinder. The cylinder was positioned at the isocenter of the commercial multisection CT scanner (Lightspeed), and a 3-cm^3 CT chamber (MDH 1015; MDH, Monrovia, Calif) was placed in the center hole to measure air kerma. At 80, 100, and 120 kVp, CT images were obtained in a series of 14 exposure levels ranging from 10 to 300 mAs. The images were acquired with the scanner by using the detail reconstruction filter (34) with a 10-cm field of view, which corresponded to pixel dimensions of 195 × 195 μm. The section thickness was 1.25 mm at the isocenter of the scanner.

For each image acquired, three regions of interest were evaluated (J.M.B., J.A.S.) by using commercially available image analysis software (EFILM; University of Toronto, Ontario, Canada). The root mean square SD (ie, noise) in each region of interest was recorded, and the average noise ($\sigma_{CT\#}$) of the three regions of interest was computed for each image. The noise was fit as a function of mAs by using the equation $\sigma_{CT\#} = a \times (mAs)^b$ with commercially available software (Freelance 97; Lotus, Cambridge, Mass), where a and b are constants. These data allowed the $\sigma_{CT\#}$ to be computed as a function of either mAs or dose for each kVp. The $\sigma_{CT\#}$ measurements allowed the denominator of the contrast-to-noise ratio (CNR) to be evaluated as a function of kVp and mAs.

Johns and Yaffe (35) measured the linear attenuation coefficients (LACs) for fibrous (ie, glandular) tissue, fat from the breast (ie, adipose tissue), and infiltrating ductal carcinoma (ie, cancer) for monoenergetic x rays ranging from 18 to 110 keV at eight different energy levels. In addition to these attenuation coefficient data, the elemental compositions of the three tissues (ie, glandular, adipose, and cancer) determined by Hammerstein et al (30) were used, and mass attenuation coefficients were computed by using the mixture rule (36) coupled with published attenuation coefficient data (37). The mass attenuation coefficients of each of the tissue types were multiplied by the physical density to compute the LAC. The computer-generated LACs for breast tissue (30,35) were used to computer fit the measured LACs reported by Johns and Yaffe (35) by using least squares techniques and letting the physical density and the relative glandular fraction vary as free parameters. Once the LAC versus monoenergetic x-ray energy was parameterized for each of the three tissue types, x-ray spectra (29) from 30 to 140 kVp were used to weight the monoenergetic LAC values to produce the effective LAC for each polyenergetic spectrum. This was done for adipose, glandular, and cancer tissues and for water. By using the LACs for each tissue type and for water, we computed the corresponding CT number (CT#), or Hounsfield unit, by using the following formula (23): $CT\# = 1{,}000 \times [(\mu_t - \mu_w)/\mu_w]$, where CT# is the CT number of the tissue with an LAC of μ_t, and μ_w is the LAC of water.

CNRs were computed by using differences in CT attenuation values as contrast and the noise measurements parameterized from experimental measurements as noise. The CNRs were converted to SNRs for different size objects by using the Rose relationship (38): $SNR = CNR \times (N)^{1/2}$, where N is the number of pixels corresponding to the breast cancer lesion. For lesion diameter d and pixel dimension Δ, $N = (\pi/4) \times (d/\Delta)^2$.

Cadaveric Breast Imaging

A cadaveric breast was acquired with proper authorization at our institution. The breast was removed from the cadaver with the pectoralis major and minor muscles attached and immediately fixed in 5% formalin. To have the breast in a more natural position during CT scanning, the pectoralis muscle with the accompanying skin flap was sutured onto stiff cardboard by using plastic ties. The breast was placed in the head holder of the clinical multisection CT scanner (Lightspeed), with the long axis of the cylinder of the breast parallel to the table motion. The breast was scanned at 80 kVp, with one acquisition at 50 mAs and without repositioning; another acquisition was performed at 80 mAs. Nonhelical CT images were acquired by using a 1.25-mm section thickness, and a 15.5 × 15.5-cm field of view was reconstructed. This resulted in pixel dimensions of 303 × 303 μm. The CT images were reconstructed by using both standard and detail reconstruction filters.

The CT images were transferred to an imaging workstation for display and analysis. Custom software that enabled the CT images to be loaded into a volume data set was written (by using Microsoft C/C++ 5.0 Compiler; Microsoft, Redmond, Wash), and coronal, transverse, and sagittal views were generated. The viewing software could average any number of adjacent images at any location in the volume to create thicker sections.

For comparison images and dosimetry, the cadaveric breast was placed under compression in a clinical mammography system and imaged by using a prototype computed radiography system (Fuji Medical, Tokyo, Japan) designed for digital mammography. The dedicated mammography imaging plate was read out by using a clinical computed radiography reader (Fuji CR 5000; Fuji Medical) with prototype software that was customized for digital mammography and used 100-μm pixels. The compressed breast thickness averaged 8.0 cm in the compression device. The mammographic radiation dose to the breast was estimated by using an 8-cm-thick phantom designed to emulate a 50% glandular, 50% adipose breast (Computerized Image Reference Systems, Norfolk, Va). This phantom was imaged by using the autofil-

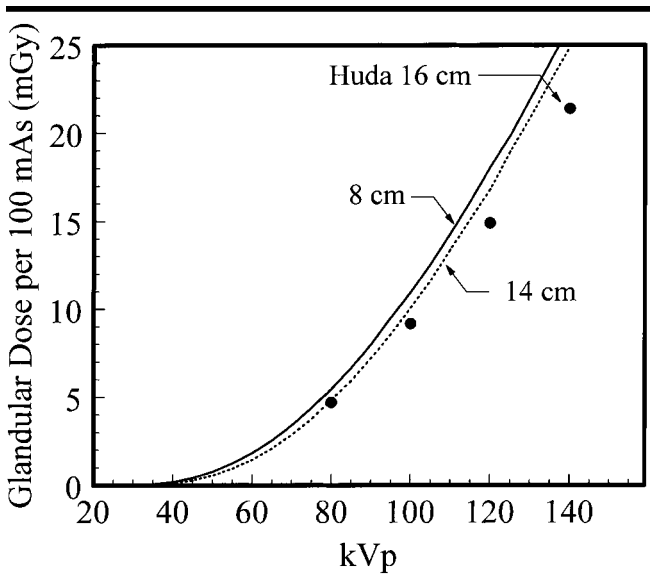

Figure 3. Graph depicts values of AGD per 100 mAs as functions of kVp, determined by using Monte Carlo techniques, for two breast diameters. There is good correlation with the published data of Huda et al (39).

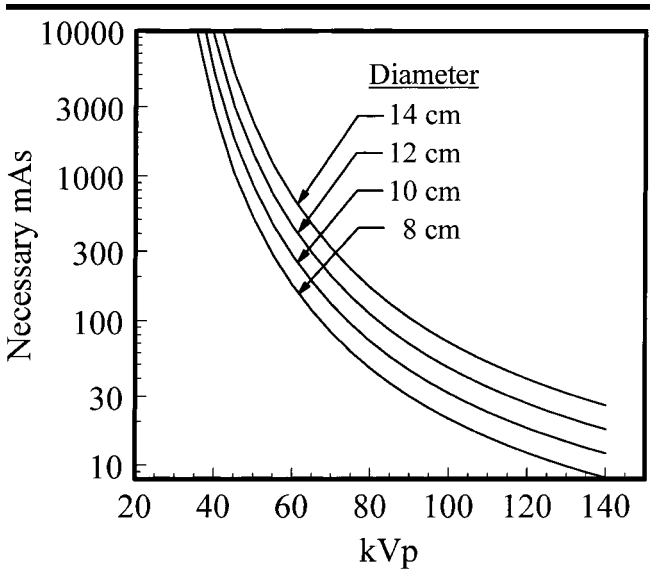

Figure 4. Graph depicts the mAs required to produce constant SNR images of 50% glandular tissue, 50% adipose tissue breasts of various diameters as functions of kVp. The mAs values shown yield the same photon fluence at the CT detector as that at a typical clinical CT examination, in which the image quality is known to be excellent.

ter mode on a Mammography Quality Standards Act–certified clinical mammography system (Lorad Mark IV; Hologic, Danbury, Conn). This system used 32 kVp and 226 mAs with a molybdenum anode and a rhodium filter. The relationship between mAs and air kerma entrance exposure to the breast was determined, and this value was used to calculate the entrance kerma to the breast. Published tables (32) were used to estimate the AGD for the cadaveric breast.

RESULTS

Breast Measurement

The average breast width (± SD) was 19.4 cm ± 2.82 and correlated poorly with breast thickness (r^2 = 0.159). Because the magnification factor was not taken into consideration, our estimates of the physical breast dimensions were slightly high (~5%). Thus, error toward more conservative higher dose estimates existed. The area of the approximately rectangular cross section of the breast during mammographic compression was assumed to be equivalent to the area of the cylindrical pendulant breast (Fig 2), and the resulting diameters of the breasts were related to breast thickness T by using the following formula: Diameter = $2 \times [(19.4 \times T)/\pi]^{1/2} = 4.97 \times (T)^{1/2}$.

Monte Carlo Simulations

The graph in Figure 3 illustrates the AGD per 100 mAs as a function of kVp. The data in this figure include the inherent inefficiencies of x-ray production at lower kVp (in terms of air kerma per mAs); these inefficiencies are compounded by the fact that 8 mm of added aluminum filtration was used at all kVps. The glandular dose per 100 mAs, which is essentially a Monte Carlo determination of the CT dose index values for breast CT, is not strongly dependent on the diameter of the breast. Data for breast diameters of 8 cm and 14 cm are shown. Data for intermediate breast diameters were computed and were between the two curves, but they are not plotted in Figure 3 for clarity. For comparison, the solid circles in Figure 3 depict the CT dose index values for a 16-cm head phantom reported by Huda et al (39). The values measured by Huda et al were converted from dose in PMMA to dose in glandular tissue values by using the ratio of mass energy attenuation coefficients. There was excellent agreement with the CT dose index values obtained by Huda et al, considering that the x-ray beam filtration and phantom diameter were slightly different.

The graph in Figure 4 illustrates the mAs, as a function of kVp, necessary to achieve good image quality at breast CT. We computed the necessary mAs at each kVp, matching the photon fluence at the CT detector array to that of a high-dose clinical examination known to produce excellent image quality. Because these data were produced by using computer simulation, no dose inefficiencies due to post patient collimation or multisection (40) detector configuration or beam geometry were included in either the abdominal or breast CT simulations. For the typical breast diameter of 10–12 cm, at 80 kVp, the mAs required to produce a high-quality breast CT image ranges from 72 to 110 mAs.

The graph in Figure 5 shows the AGD necessary to produce a 1-mm breast CT

section with good image quality. The data in Figure 5 are the product of the curves (at the same breast diameters) illustrated in Figures 3 and 4 with proper normalization. Breast CT requires only one acquisition, whereas screening mammography performed in the United States makes use of two nearly orthogonal projections. Whereas the dose for breast CT at low kVp is extremely high, at 80 or 100 kVp, the dose for breast CT is comparable to that for two-view mammography. For example, a 4.5-cm-thick compressed breast may receive an AGD of nearly 2.0 mGy per view at mammography, for a total dose of 4.0 mGy. The corresponding breast CT diameter is 10.5 cm, and at 80 kVp, the AGD for breast CT also is about 4.0 mGy. The data in Figure 5 demonstrate that women with larger breasts receive larger doses at breast CT and were calculated with the assumption that the mAs increases as the breast diameter increases to maintain a constant image SNR. The automatic exposure control systems on mammography machines increase the entrance kerma for larger breasts as well; therefore, women with larger breasts receive larger x-ray doses at mammography. Thus, for both mammography and breast CT, radiation dose increases with breast size.

The graph in Figure 6 shows a comparison of AGD versus breast thickness at two-view mammography and breast CT. The "UCD mammo" curve represents doses computed by using the clinical techniques appropriate for each breast thickness at the University of California, Davis Medical Center. The published values of Wu (41) for 25- and 30-kVp mammography also are shown and compare well with the University of California, Davis Medical Center results when the differences in kVp are considered. The calculated breast CT doses are shown with 95% CIs (± 2 SDs). For breasts larger than about 5 cm, breast CT at 80 kVp was shown to deliver a lower breast dose than mammography. The median breast thickness determined from the analysis in 82 women was 5.2 cm, so about 50% of women had breasts larger than 5 cm. The dose benefit of breast CT increased for women with breasts larger than the median. For example, the breast CT dose at 80 kVp for a 6-cm-thick, 50% glandular breast—5.8 mGy—was 26% lower than that for two-view mammography—7.8 mGy. For an 8-cm-thick breast, the CT dose—8.3 mGy—was 29% lower than that for mammography—11.6 mGy. The radiation dose levels for CT at 100 and 120 kVp were are even lower. The coefficient of variation of the breast CT doses (averaged across the breast diameters) were 0.44%, 0.51%, and 0.39%, for the 80-, 100-, and 120-kVp data, respectively.

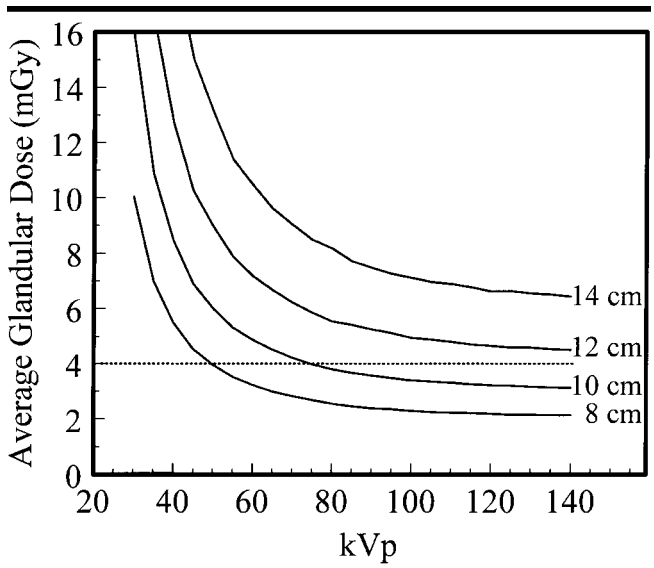

Figure 5. Graph depicts AGD values, as functions of kVp, for four breast diameters. The data are the product of the data shown in Figures 3 and 4, with proper normalization. The typical dose for two-view mammography of a 4-cm compressed breast, which corresponds to a 10-cm-diameter breast at CT, is illustrated by the dashed line. The CT dose is comparable to that at two-view mammography.

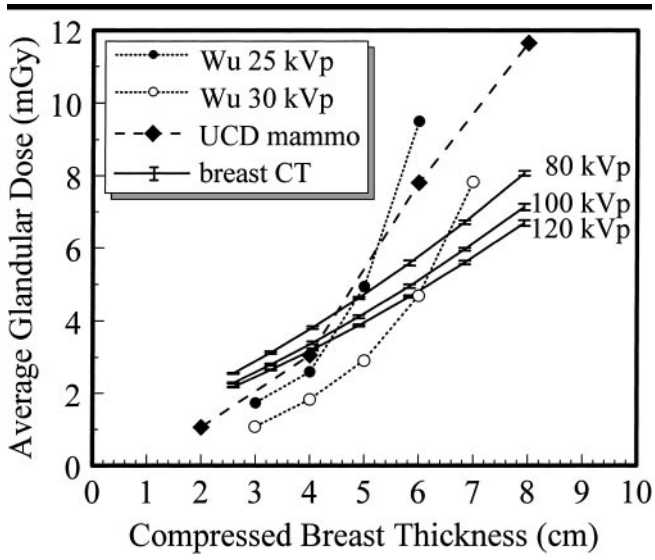

Figure 6. Graph depicts AGD values as functions of compressed breast thickness for two-view mammography and breast CT. The doses computed at 25 and 30 kVp by Wu (41) are shown for comparison. The University of California, Davis Medical Center mammographic (*UCD mammo*) data reflect realistic clinical mammography doses measured at our institution. The breast CT doses (shown with 95% CIs) are lower than the two-view mammography doses for breasts larger than 5 cm and are only slightly higher for smaller breasts.

The AGD has become the standard metric value used to assess dose at mammography; however, this parameter masks the large spatial differences in radiation dose to the breast that occur during mammography. Monte Carlo techniques were used to evaluate the dose distributions at both breast CT and two-view mammography. The CT dose profiles illustrated in Figure 7 show that the dose to the breast during breast CT was very homogeneous. The 80-kVp breast CT

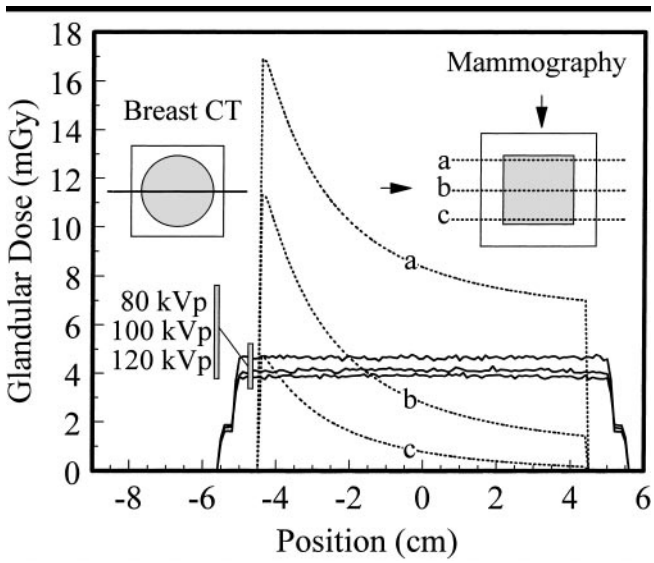

Figure 7. Graph illustrates the distributions of glandular dose as functions of position for both mammography and breast CT. The breast CT dose profiles demonstrate a virtually homogeneous distribution of dose to each voxel in the breast, and this is a consequence of the source rotating around the breast during CT acquisition. The combination of the nearly orthogonal craniocaudal and mediolateral oblique views results in the markedly heterogeneous dose distribution at mammography. The dotted lines labeled *a, b,* and *c* on the graph correspond to the positions shown on the inset for mammography.

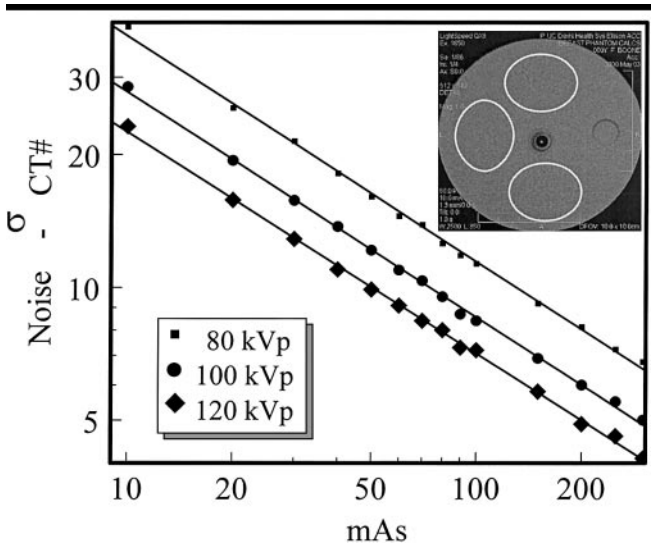

Figure 8. Graph illustrates $\sigma_{CT\#}$ (ie, noise) in the CT number of a 10-cm-diameter PMMA cylinder as functions of mAs for three kVp settings. The SDs were determined from three elliptical regions of interest on the CT images, as indicated on the box inset. The graph is shown with logarithmic axes, and the slope of each best-fit line is −½, which is consistent with the dose-limited performance of the scanner. These data were used to characterize the noise on the image as a function of mAs and kVp.

doses were slightly higher than the doses at 100 and 120 kVp, and this was expected since the mAs setting at 80 kVp was increased to maintain the SNR.

The dose distribution for mammography also is shown in Figure 7. The corner of the breast that was near the entrance x-ray beams for both the craniocaudal and mediolateral oblique views received the highest dose, whereas the opposite corner received the lowest dose. Although the AGD to a 5-cm breast at breast CT is very similar to that at mammography, there is a huge amount of spatial variation in the dose delivered to the breast at mammography. Quantitative analysis of the dose histograms for two-view mammography indicated that 5% of the breast received an average of 14.2 mGy (1.4 rad) and 20% of the breast received an AGD greater than 10 mGy (1 rad). This is not surprising, given the low x-ray energy levels and high attenuation levels that are typical for mammography.

Experimental Results

The CT image noise for a 10-cm PMMA phantom is illustrated in Figure 8. The box inset is a CT image of the phantom with the positions of the three regions of interest that were used to compute the noise. The $\sigma_{CT\#}$ was greater at a low mAs setting, as expected, and at the same mAs setting, the $\sigma_{CT\#}$ was higher at lower kVp, indicating a reduced number of x-ray photons reaching the detector at lower kVp. The power regression lines ($\sigma_{CT\#} = a[\text{mAs}]^b$, where a and b are constants) with use of the least squares criterion for fitting demonstrated excellent correlation with the measured data points, with r^2 values of 0.998, 0.998, and 0.999, for the 80-, 100-, and 120-kVp curves, respectively. The slopes of these log-log curves were determined to be essentially −½ (mean ± SD, −0.508 ± 0.0055), which is consistent with the quantum limited behavior of the CT scanner, where $\sigma_{CT\#} = a(\text{mAs})^{-1/2}$, with a as a constant of proportionality. The data shown in Figure 8 allowed the parameterization of noise versus mAs and of noise versus dose, which was useful for subsequent computation of the CNR versus dose and the SNR versus dose.

Relevant LACs for polyenergetic CT spectra are illustrated as functions of kVp in Figure 9. The contrast of cancer on a CT image is the numerical difference between the CT number of cancer and that of the background tissue (adipose or glandular tissue).

The CNRs calculated as functions of AGD to the breast at 80, 100, and 120 kVp are illustrated in Figure 10. The CNR for breast cancer against an adipose tissue background is shown in Figure 10a, and the CNR for breast cancer against a glandular tissue background is shown in Figure 10b. At a dose of 4 mGy (ie, for two-view mammography of a typical breast), the CNR at 80 kVp is 14.5 for cancer against an adipose tissue background (Fig 10a) and

1.85 for cancer against a glandular tissue background (Fig 10b).

The SNRs of breast lesions against a glandular tissue background, calculated from CNRs and pixel counts per lesion, are shown in Figure 11. This calculation was performed with the assumption of a homogeneous breast tissue background in which the anatomic (ie, structure) noise that resulted from normal breast parenchyma was considered negligible. The actual SNR would be lower owing to the presence of anatomic noise.

Cadaveric Breast CT

After scanning the cadaveric breast at 50 and 80 mAs, we realized that this breast was larger than the average breast and thus a higher mAs setting should have been used. Because the 50- and 80-mAs acquisitions were performed without repositioning, it was possible to simply average both image sets, image by image, to synthesize CT images equivalent to those obtained with 130-mAs acquisition at 80 kVp. Four selected coronal CT images of the cadaveric breast are shown in Figure 12. The estimated AGD at CT was 6.32 mGy for this relatively large breast. As the scanning plane approached the posterior region of the cadaveric breast specimen, dark regions on the image that corresponded to air pockets were visible. Such artifacts are a consequence of using a cadaveric breast and would not be a factor in live women. The mammographic radiation dose for this 8-cm-thick breast was estimated to be 5.06 mGy for the craniocaudal view; thus, for standard two-view mammography, the total AGD would be 10.1 mGy. In comparison, the breast CT dose to this breast was estimated to be 6.32 mGy. Therefore, the CT images shown in Figure 12 were acquired with a 37% lower mean glandular dose compared with the dose delivered at two-view mammography.

A digital mammogram of the cadaver breast is illustrated in Figure 13, *A*. The CT volume data set was used to generate a digital mammogram, albeit of low spatial resolution, and this image is illustrated in Figure 13, *B*. Other than the difference in spatial resolution and the lack of compression in the CT data, the calculated projection image through the CT data set is similar in overall appearance to the mammogram. For comparison, a breast CT image reformatted to the transverse projection is shown in Figure 13, *C*; the ductal structures that are visible on this image are impossible to discern on the other two images. The three images in Figure 13 demonstrate the exceptional tissue contrast

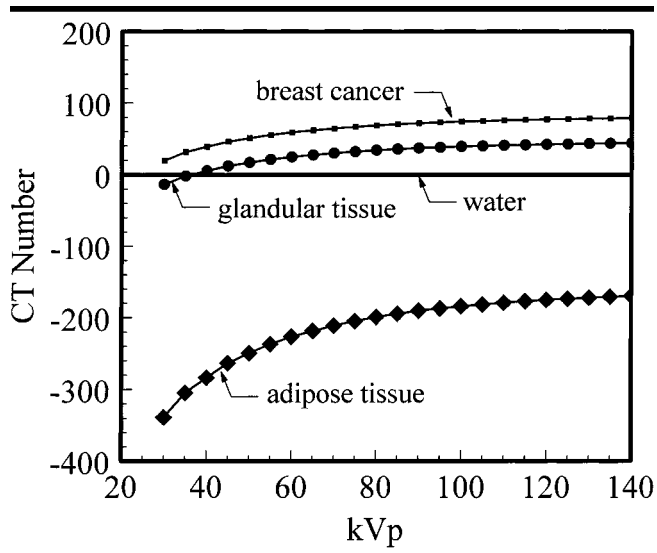

Figure 9. Graph illustrates the CT numbers for breast cancer, glandular tissue, adipose tissue, and water, weighted for different kVps.

that tomographic images of the breast can provide. The CT images, when overlaid on each other to simulate a projection image, have the same structure noise problems as is evident in the mammogram. This suggests that the problems concerning mammography of dense breasts that are frequently mentioned in the literature (14–16) are mainly due to the complicated overlapping structures and secondarily related to the mode of detection.

DISCUSSION

Radiation dose to the breast is a crucial issue in the context of breast CT feasibility. Figure 6 shows a comparison of breast CT dose versus AGD at two-view mammography. The data show that breast CT involves lower doses than does mammography for breasts thicker than 5 cm. Although the data shown are experimental, the mammographic doses are well established and the CT dose computations are consistent with published CT dose index values.

Compare the typical mammographic setting of a 5-cm compressed breast imaged with 26 kVp and a molybdenum/molybdenum x-ray beam with the setting of an 11-cm-diameter breast imaged with an 80-kVp x-ray beam, as proposed for breast CT (33,37). For 1,000 input photons to the breast, 14 primary photons emerge at mammography, as compared with 90 primary photons that emerge at breast CT—a 6.3-fold increase in photon penetration. In terms of energy fluence, for a spectrum with an entrant energy fluence of 1,000 keV (integral of entire spectrum), 17 keV of primary radiation emerges from the breast at mammography, as compared with 96 keV at breast CT—better x-ray energy penetration by a factor of 5.8. CT is a high-SNR imaging technique that requires relatively high photon fluence to the detectors; however, the higher beam energy and commensurate increase in penetrability of the proposed breast CT spectrum more than compensate for the high fluence requirements of CT. The results of this research demonstrate that high-quality breast CT can be performed at dose levels that are equivalent to or lower than those used in present-day mammography.

The dose homogeneity of breast CT is far greater than that of mammography. For nearly identical AGD values, the peak dose levels for an appreciable portion of the breast are far higher at mammography than the peak levels at breast CT. If radiation risk is truly a linear no-threshold phenomenon, as assumed by regulatory bodies, then the risks at mammography and breast CT are equivalent. However, if radiation risk is a nonlinear function of dose, as some radiobiologic data suggest (42), then the radiation risk with breast CT is lower than that with mammography due to the greater dose homogeneity.

In addition to using well-validated (27,28) Monte Carlo studies, we performed experimental measurements of the noise properties of breast CT, and published data were used to evaluate the contrast properties of this modality. On the basis of the combined contrast and noise data, the CNRs and corresponding SNRs for small

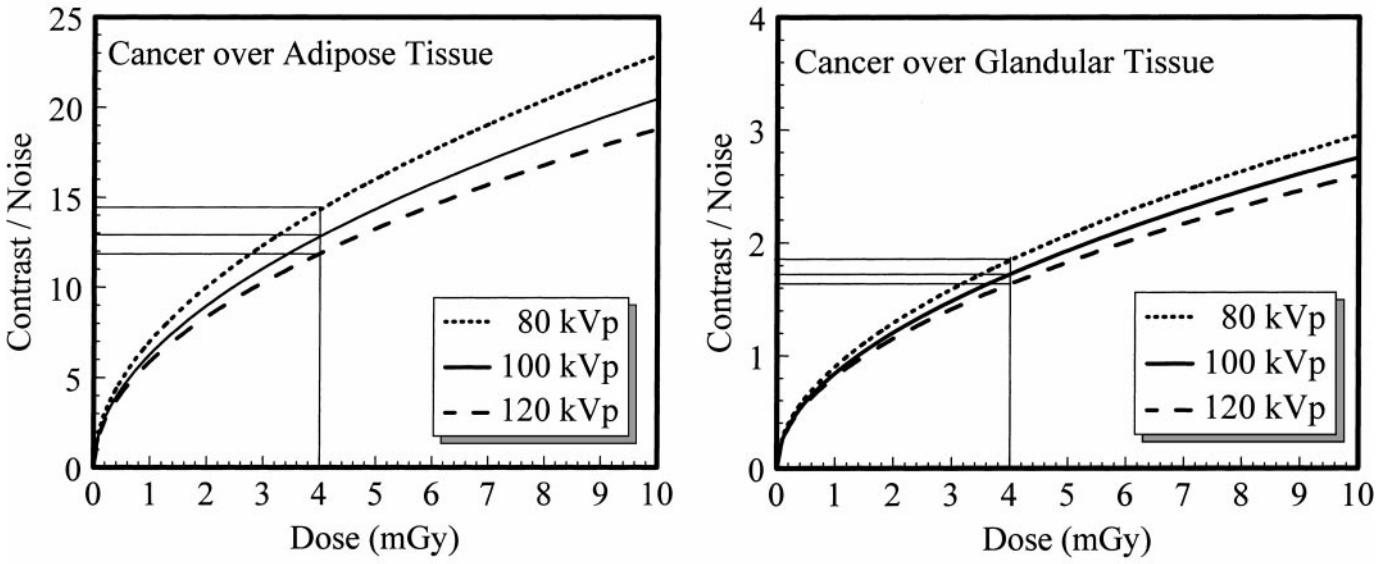

a. b.

Figure 10. **(a)** Graph illustrates CNRs of a breast cancer lesion against an adipose tissue background as functions of dose for breast CT. At a dose of 4 mGy, the CNR is about 14 at 80 kVp. **(b)** Graph illustrates CNRs of a breast cancer lesion against a glandular tissue background as functions of dose for breast CT. At a dose of 4 mGy, the CNR per pixel is approximately 2.5.

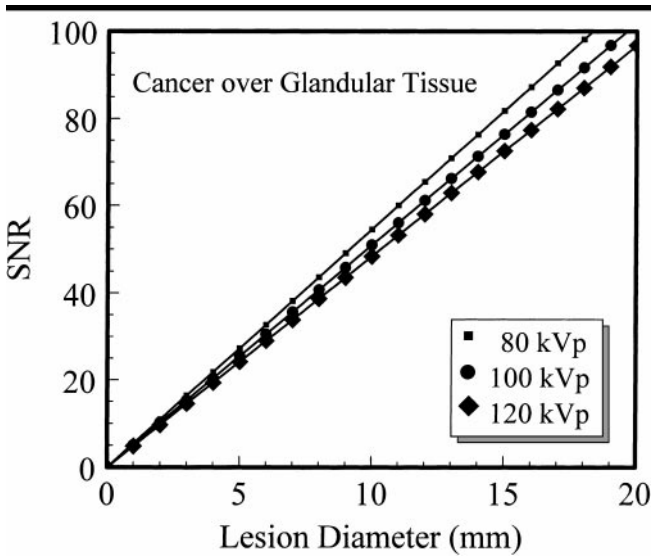

Figure 11. Graph depicts SNRs of a breast cancer lesion positioned in a glandular breast tissue background as functions of lesion diameter. These data were calculated with the assumption of 300 × 300-μm pixels, a detail reconstruction filter, and an AGD of 4 mGy delivered to a 10-cm-diameter breast. The SNRs shown demonstrate, on the basis of the Rose criterion, that high-SNR CT images can be acquired at clinically acceptable doses.

breast cancer lesions are impressive. According to the Rose criterion (43), an object will almost certainly be detected if the SNR exceeds 5, and with use of this criterion, lesions as small as 2 or 3 mm in diameter may be easily detected at breast CT. In comparison, the median lesion diameter detected by using screen-film mammography has been reported to be between 11 and 16 mm (44–46). These calculations are for the simple case in which the image background surrounding the lesion is homogeneous, which is not the case with most breast imaging studies. This is where the power of tomography comes to play: Because of the reduced overlapping normal anatomy, the image background of breast CT (Fig 13) is far more homogeneous than that of mammography, in which overlapping breast parenchyma produces a very complicated normal breast background. The problem is worse with dense breasts. For an 11-cm-diameter (median) breast and transversely formatted sections, the acquisition of 1-mm-thick CT sections would reduce the volume of underlying and overlying tissue by a factor of 110.

Whereas the amount of structured noise that the approximately 100 out-of-plane sections contribute to the projection image (but not to the CT section) depends on the distribution of breast density, the combination of the improved SNR and the approximately 10-fold reduction in structured noise (~100-fold reduction in variance) suggests that the performance of breast CT in early breast cancer detection may be impressive.

Digital tomosynthesis is a limited angle tomographic technique that has been studied for use in breast cancer screening (47,48). Although tomosynthesis is extremely promising, its potential for mammography has yet to be fully understood. It is likely that dedicated breast CT will result in substantially less structured noise than will tomosynthesis due to the much thinner tomographic sections that are produced at CT. Tomosynthesis will likely provide better spatial resolution but worse contrast resolution than CT and likely provide lower spatial resolution but better contrast resolution than mammography of the dense breast. What the optimum tradeoff is between these parameters for

clinical cancer detection remains to be studied.

Breast compression is a necessity at mammography; however, many women are very apprehensive about the compression and hence the mammographic examination (49–51). With breast CT, compression is not needed to produce high-quality images, and, given the rotational acquisition requirements of CT, conventional compression cannot be used to an advantage anyway. Because compression is not required for breast CT, this examination may be better tolerated by some women than is mammography.

The finding of microcalcifications is the sole basis of the diagnosis in a minority (~19%) of breast cancer cases (52), and how well breast cancers with microcalcifications can be detected using breast CT remains to be seen. With flat-panel cone-beam acquisition techniques, it would be possible during CT scanning to produce images with higher spatial resolution for microcalcification detection than the reconstructed CT images. The fundamental importance of microcalcification detection in cancer screening may be overestimated because this is the diagnostic area in which mammography excels. More research is warranted, but it is possible that improvements in contrast resolution, with slight compromises in spatial resolution, may yield better overall cancer detection rates.

According to the Rose criterion (53), objects will be seen with high confidence when their SNR is greater than about 5. The data in Figure 11 demonstrate that a 1-mm breast cancer lesion lying against a glandular tissue background has a SNR of about 5. It is likely, however, that when the added anatomic noise is included, SNR levels will decrease and slightly larger lesions will be required to reach a SNR of 5—the point where they would be easily detected. If breast CT was able to achieve a median lesion detection level of 5 mm, for example, this would advance early detection by 0.93 years compared with 11-mm lesions, as at mammography, assuming a doubling time of 100 days (54). A median detectable lesion size of 3 mm would result in a 1.5-year advantage in earlier detection. The potential for much earlier detection has important applications for reducing the morbidity and mortality of breast cancer. For example, a 5-mm-diameter lesion has 9.4% of the cell count of an 11-mm lesion, and a 3-mm-diameter lesion has only 2% of the cells of an 11-mm tumor.

In summary, it has been a general perception for more than 2 decades that the radiation dose at breast CT would prohibit its use for breast screening. In this investigation, the radiation dose delivered in the proposed breast CT scanner design was comparable to or lower than the doses delivered at routine mammography. In addition, analysis of phantom CT images revealed that the CNR and SNR of breast

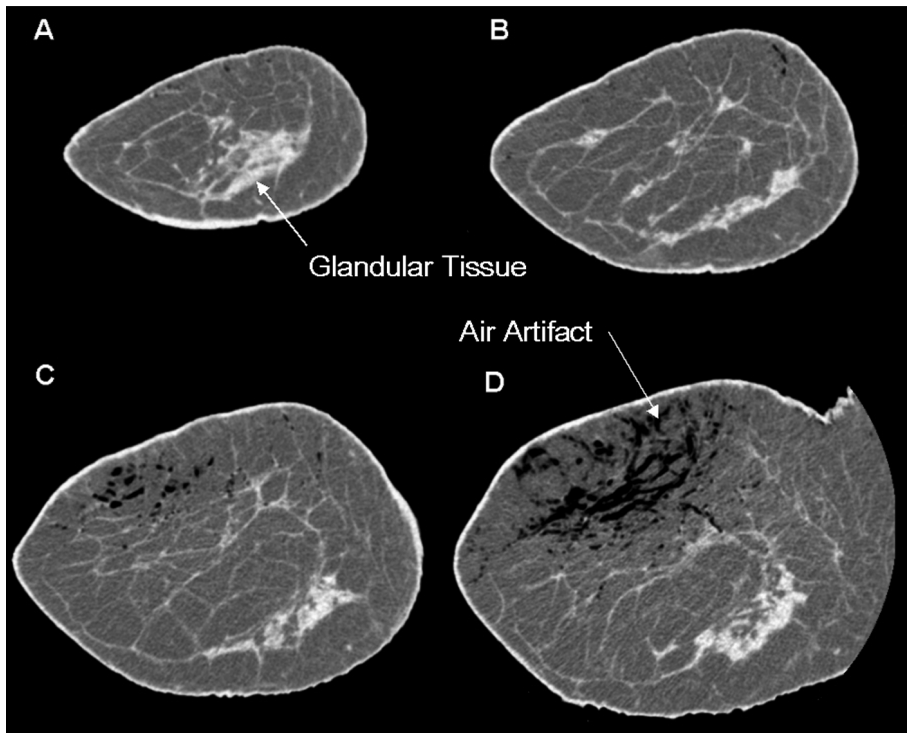

Figure 12. Coronal CT images of the cadaveric breast acquired in the anterior to posterior *(A–D)* planes with a clinical CT scanner by using 80 kVp and the equivalent of 130 mAs, with a section thickness of 1.25 mm and pixel dimensions of 303 × 303 μm. The detail reconstruction filter was used. These images demonstrate far greater tissue contrast than that seen on mammograms. The air artifacts are the result of breast fixation and storage.

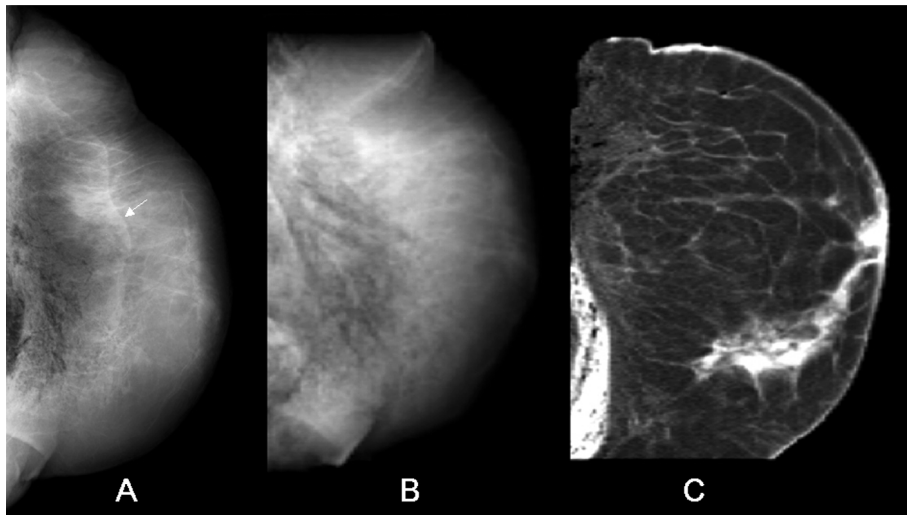

Figure 13. *A,* Digital mammogram of cadaveric breast. *B,* Projection mammogram constructed by using CT data set. The coronal CT sections were reformatted to the transverse plane to create a transverse CT section *(C)* of the middle portion of the breast. It is apparent that the depiction of contrast in the breast image is related less to the mode of detection and more to the presence of overlying tissue (as in *A* and *B*) that substantially obscures visualization of the anatomic structure (and probably the breast cancer) in the breast. The fixation fluid produced a line artifact (arrow in *A*) when the breast was compressed for mammography.

cancer would be high at reasonable dose levels. The coronal CT images of a cadaveric specimen acquired at dose levels lower than those used at mammography were promising at subjective inspection; however, clinical studies are needed to scientifically evaluate the potential of breast CT for breast cancer screening. In our opinion, breast CT technology with modern detector systems should be developed so that such studies can be implemented.

References

1. Tabar L, Chen HH, Fagerberg G, Duffy SW, Smith TC. Recent results from the Swedish Two-County Trial: the effects of age, histologic type, and mode of detection on the efficacy of breast cancer screening. J Natl Cancer Inst Monogr 1997; 22:43–47.
2. Larsson LG, Andersson I, Bjurstam N, et al. Updated overview of the Swedish Randomized Trials on Breast Cancer Screening with Mammography: age group 40–49 at randomization. J Natl Cancer Inst Monogr 1997; 22:57–61.
3. Larsson LG, Nystrom L, Wall S, et al. The Swedish randomised mammography screening trials: analysis of their effect on the breast cancer related excess mortality. J Med Screen 1996; 3:129–132.
4. Kakuda JT, Stuntz ME, Vargas HI, Khalkhali I. Status of scintimammography and its relationship to other detection methods for breast cancer. Cancer Biother Radiopharm 1999; 14:435–442.
5. Yutani K, Shiba E, Kusuoka H, et al. Comparison of FDG-PET with MIBI-SPECT in the detection of breast cancer and axillary lymph node metastasis. J Comput Assist Tomogr 2000; 24:274–280.
6. Rostom AY, Powe J, Kandil A, et al. Positron emission tomography in breast cancer: a clinicopathological correlation of results. Br J Radiol 1999; 72:1064–1068.
7. Flanagan FL, Dehdashti F, Siegel BA. PET in breast cancer. Semin Nucl Med 1998; 28:290–302.
8. Coons TA. MRI's role in assessing and managing breast disease. Radiol Technol 1996; 67:311–336.
9. Morris EA, Schwartz LH, Dershaw DD, Van Zee KJ, Abramson AF, Liberman L. MR imaging of the breast in patients with occult primary breast carcinoma. Radiology 1997; 205:437–440.
10. Manoharan R, Shafer K, Perelman L, et al. Raman spectroscopy and fluorescence photon migration for breast cancer diagnosis and imaging. Photochem Photobiol 1998; 67:15–22.
11. Hagness SC, Taflove A, Bridges JE. Two-dimensional FDTD analysis of a pulsed microwave confocal system for breast cancer detection: fixed-focus and antenna-array sensors. IEEE Trans Biomed Eng 1998; 45:1470–1479.
12. Jackson VP, Reynolds HE, Hawes DR. Sonography of the breast. Semin Ultrasound CT MR 1996; 17:460–475.
13. Bird RE, Wallace TW, Yankaskas BC. Analysis of cancers missed at screening mammography. Radiology 1992; 184:613–617.
14. Swann CA, Kopans DB, McCarthy KA, White G, Hall DA. Mammographic density and physical assessment of the breast. AJR Am J Roentgenol 1987; 148:525–526.
15. Jackson VP, Hendrick RE, Feig SA, Kopans DB. Imaging of the radiographically dense breast. Radiology 1993; 188:297–301.
16. Sabol JM, Soutar IC, Plewes DB. Mammographic scanning equalization radiography. Med Phys 1993; 20:1505–1515.
17. Pisano ED, Parham CA. Digital mammography, sestamibi breast scintigraphy, and positron emission tomography breast imaging. Radiol Clin North Am 2000; 38: 861–869.
18. Simonetti G, Cossu E, Montanaro M, Caschili C, Giuliani V. What's new in mammography. Eur J Radiol 1998; 27(suppl 2):S234–S241.
19. Chang CH, Sibala JL, Fritz SL, Dwyer SJ, Templeton AW. Specific value of computed tomographic breast scanner (CT/M) in diagnosis of breast diseases. Radiology 1979; 132:647–652.
20. Gisvold JJ, Reese DF, Karsell PR. Computed tomographic mammography (CTM). AJR Am J Roentgenol 1979; 133:1143–1149.
21. John V, Ewen K. CT scanning of the breast in problem cases. Strahlenther Onkol 1989; 165:657–662.
22. Chang CH, Nesbit DE, Fisher DR, et al. Computed tomographic mammography using a conventional body scanner. AJR Am J Roentgenol 1982; 138:553–558.
23. Bushberg JT, Seibert JA, Leidholdt EM, Boone JM. The essential physics of medical imaging. Baltimore, Md: Williams & Wilkins, 1994.
24. Siewerdsen JH, Jaffray DA. Cone-beam computed tomography with a flat-panel imager: effects of image lag. Med Phys 1999; 26:2635–2647.
25. Antonuk LE, Jee KW, El Mohri Y, et al. Strategies to improve the signal and noise performance of active matrix, flat-panel imagers for diagnostic x-ray applications. Med Phys 2000; 27:289–306.
26. Siewerdsen JH, Antonuk LE, El Mohri Y, Yorkston J, Huang W, Cunningham IA. Signal, noise power spectrum, and detective quantum efficiency of indirect-detection flat-panel imagers for diagnostic radiology. Med Phys 1998; 25:614–628.
27. Boone JM, Buonocore MH, Cooper VN. Monte Carlo validation in diagnostic radiological imaging. Med Phys 2000; 27: 1294–1304.
28. Boone JM, Cooper VN. Scatter/primary in mammography: Monte Carlo validation. Med Phys 2000; 27:1818–1831.
29. Boone JM, Seibert JA. An accurate method for computer-generating tungsten anode x-ray spectra from 30 kV to 140 kV. Med Phys 1997; 24:1661–1670.
30. Hammerstein GR, Miller DW, White DR, Masterson ME, Woodard HQ, Laughlin JS. Absorbed radiation dose in mammography. Radiology 1979; 130:485–491.
31. Knox HH, Gagne RM. Alternative methods of obtaining the computed tomography dose index. Health Phys 1996; 71:219–224.
32. Boone JM. Glandular breast dose for monoenergetic and high-energy x-ray beams: Monte Carlo assessment. Radiology 1999; 213:23–37.
33. Boone JM, Fewell TR, Jennings RJ. Molybdenum, rhodium, and tungsten anode spectral models using interpolating polynomials with application to mammography. Med Phys 1997; 24:1863–1874.
34. Brooks RA, Di Chiro G. Theory of image reconstruction in computed tomography. Radiology 1975; 117:561–572.
35. Johns PC, Yaffe MJ. X-ray characterisation of normal and neoplastic breast tissues. Phys Med Biol 1987; 32:675–695.
36. Boone JM. X-ray production, interaction, and detection in diagnostic imaging. In: Beutel J, Kundel HL, Van Metter RL, eds. Handbook of medical imaging. Bellingham, Wash: SPIE, 2000; 1–78.
37. Boone JM, Chavez AE. Comparison of x-ray cross sections for diagnostic and therapeutic medical physics. Med Phys 1996; 23:1997–2005.
38. Hasegawa BH. The physics of medical x-ray imaging. Madison, Wis: Medical Physics, 1991.
39. Huda W, Atherton JV, Ware DE, Cumming WA. An approach for the estimation of effective radiation dose at CT in pediatric patients. Radiology 1997; 203:417–422.
40. McCollough CH, Zink FE. Performance evaluation of a multi-slice CT system. Med Phys 1999; 26:2223–2230.
41. Wu X. Breast dosimetry in screen film mammography. In: Barnes GT, Frey GD, eds. Screen film mammography: imaging considerations and medical physics responsibilities. Madison, Wis: Medical Physics, 1991; 159–175.
42. Rossi HH. Radiation physics and radiobiology. Health Phys 1996; 70:828–831.
43. Burgess AE. The Rose model, revisited. J Opt Soc Am A Opt Image Sci Vis 1999; 16:633–646.
44. Curpen BN, Sickles EA, Sollitto RA, Ominsky SH, Galvin HB, Frankel SD. The comparative value of mammographic screening for women 40–49 years old versus women 50–64 years old. AJR Am J Roentgenol 1995; 164:1099–1103.
45. Arnesson LG, Vitak B, Manson JC, Fagerberg G, Smeds S. Diagnostic outcome of repeated mammography screening. World J Surg 1995; 19:372–377.
46. Thurfjell E. Mammography screening methods and diagnostic results. Acta Radiol Suppl 1995; 395:1–22.
47. Niklason LT, Christian BT, Niklason LE, et al. Digital tomosynthesis in breast imaging. Radiology 1997; 205:399–406.
48. Webber RL, Underhill HR, Freimanis RI. A controlled evaluation of tuned-aperture computed tomography applied to digital spot mammography. J Digit Imaging 2000; 13:90–97.
49. Kashikar-Zuck S, Keefe FJ, Kornguth P, Beaupre P, Holzberg A, Delong D. Pain coping and the pain experience during mammography: a preliminary study. Pain 1997; 73:165–172.
50. Aro AR, Absetz-Ylostalo P, Eerola T, Pamilo M, Lonnqvist J. Pain and discomfort during mammography. Eur J Cancer 1996; 32A:1674–1679.
51. Kornguth PJ, Keefe FJ, Conaway MR. Pain during mammography: characteristics and relationship to demographic and medical variables. Pain 1996; 66:187–194.
52. Tabar L. Radiology of minimal breast cancer. Radiology 2000; 217(P):54.
53. Rose A. Vision: human and electronic. New York, NY: Plenum, 1974.
54. Spratt JS, Greenberg RA, Heuser LS. Geometry, growth rates, and duration of cancer and carcinoma in situ of the breast before detection by screening. Cancer Res 1986; 46:970–974.